Atmos. Chem. Phys., 23, 13869–13882, 2023
https://doi.org/10.5194/acp-23-13869-2023

Atmospheric Chemistry and Physics
Open Access

Technical note: Gas-phase nitrate radical generation via irradiation of aerated ceric ammonium nitrate mixtures

Andrew T. Lambe[1], Bin Bai[2], Masayuki Takeuchi[3], Nicole Orwat[4], Paul M. Zimmerman[4], Mitchell W. Alton[1], Nga L. Ng[2,3,5], Andrew Freedman[1], Megan S. Claflin[1], Drew R. Gentner[6,7], Douglas R. Worsnop[1], and Pengfei Liu[2]

[1]Aerodyne Research, Inc., Billerica, MA, USA
[2]School of Earth and Atmospheric Sciences, Georgia Institute of Technology, Atlanta, GA, USA
[3]School of Civil and Environmental Engineering, Georgia Institute of Technology, Atlanta, GA, USA
[4]Department of Chemistry, University of Michigan, Ann Arbor, MI, USA
[5]School of Chemical and Biomolecular Engineering, Georgia Institute of Technology, Atlanta, GA, USA
[6]Department of Chemical and Environmental Engineering, Yale University, New Haven, CT, USA
[7]School of the Environment, Yale University, New Haven, CT, USA

Correspondence: Andrew T. Lambe (lambe@aerodyne.com)

Received: 7 July 2023 – Discussion started: 21 July 2023
Revised: 21 September 2023 – Accepted: 21 September 2023 – Published: 7 November 2023

Abstract. We present a novel photolytic source of gas-phase NO_3 suitable for use in atmospheric chemistry studies that has several advantages over traditional sources that utilize $NO_2 + O_3$ reactions and/or thermal dissociation of dinitrogen pentoxide (N_2O_5). The method generates NO_3 via irradiation of aerated aqueous solutions of ceric ammonium nitrate (CAN, $(NH_4)_2Ce(NO_3)_6$) and nitric acid (HNO_3) or sodium nitrate ($NaNO_3$). We present experimental and model characterization of the NO_3 formation potential of irradiated CAN / HNO_3 and CAN / $NaNO_3$ mixtures containing $[CAN] = 10^{-3}$ to 1.0 M, $[HNO_3] = 1.0$ to 6.0 M, $[NaNO_3] = 1.0$ to 4.8 M, photon fluxes (I) ranging from 6.9×10^{14} to 1.0×10^{16} photons $cm^{-2}\,s^{-1}$, and irradiation wavelengths ranging from 254 to 421 nm. NO_3 mixing ratios ranging from parts per billion to parts per million by volume were achieved using this method. At the CAN solubility limit, maximum $[NO_3]$ was achieved using $[HNO_3] \approx 3.0$ to 6.0 M and UVA radiation ($\lambda_{max} = 369$ nm) in CAN / HNO_3 mixtures or $[NaNO_3] \geq 1.0$ M and UVC radiation ($\lambda_{max} = 254$ nm) in CAN / $NaNO_3$ mixtures. Other reactive nitrogen (NO_2, N_2O_4, N_2O_5, N_2O_6, HNO_2, HNO_3, HNO_4) and reactive oxygen (HO_2, H_2O_2) species obtained from the irradiation of ceric nitrate mixtures were measured using a NO_x analyzer and an iodide-adduct high-resolution time-of-flight chemical ionization mass spectrometer (HR-ToF-CIMS). To assess the applicability of the method for studies of NO_3-initiated oxidative aging processes, we generated and measured the chemical composition of oxygenated volatile organic compounds (OVOCs) and secondary organic aerosol (SOA) from the β-pinene + NO_3 reaction using a Filter Inlet for Gases and AEROsols (FIGAERO) coupled to the HR-ToF-CIMS.

1 Introduction

The importance of NO_3 as a nighttime atmospheric oxidant is well established (Wayne et al., 1991; Brown and Stutz, 2012; Ng et al., 2017; Wang et al., 2023). NO_3 is generated via the reaction $NO_2 + O_3 \rightarrow NO_3 + O_2$, followed by achievement of temperature-dependent equilibrium between NO_3, NO_2, and dinitrogen pentoxide (N_2O_5). N_2O_5 also hydrolyzes efficiently to HNO_3 on aqueous surfaces (Brown et al., 2004). Thus, any investigation of the influence of NO_3 chemistry in a specific source region necessarily must account for the local temperature, humidity, and particle surface area along with other factors. Despite these complications, for decades, laboratory studies investigating gas-phase NO_3 chemistry have utilized the same

$NO_2 + O_3$ reactions and/or N_2O_5 thermal decomposition to produce NO_3 as it occurs in the atmosphere and accommodated the inherent limitations associated with N_2O_5, namely, that it must be stored under cold and dry conditions until use. Few viable alternative methods for the generation of gas-phase NO_3 have been identified. Reactions between fluorine atoms and nitric acid ($F + HNO_3 \rightarrow HF + NO_3$) or chlorine atoms and chlorine nitrate ($Cl + ClNO_3 \rightarrow Cl_2 + NO_3$) require handling and/or synthesizing hazardous halogen-containing compounds (Burrows et al., 1985; Bedjanian, 2019). F and Cl can also compete with NO_3 for the oxidation of target analytes, as can O_3 if its reaction with NO_2 is used as the NO_3 source.

In the 1960s and 1970s, following earlier research into the properties of ceric solutions (Meyer and Jacoby, 1901; Wylie, 1951; Hinsvark and Stone, 1956; Blaustein and Gryder, 1957), Thomas Martin and coworkers discovered that irradiating solutions containing ceric ammonium nitrate (CAN, $(NH_4)_2Ce(NO_3)_6$) generates aqueous NO_3 (Henshall, 1963; Martin et al., 1963, 1964; Glass and Martin, 1970; Martin and Glass, 1970; Martin and Stevens, 1978). In $\gtrsim 6$ M nitric acid (HNO_3), CAN is thought to dissociate primarily into NH_4^+ cations and hexanitratocerate ($Ce(NO_3)_6^{2-}$) anions (Henshall, 1963). The $Ce(NO_3)_6^{2-}$ is subsequently reduced to $Ce(NO_3)_5^{2-}$ upon irradiation by ultraviolet light, and NO_3 is generated as a primary photolysis product. A similar process occurs in other solvents, although the ensuing ceric composition in solution is complex and influenced by several factors. For example, in glacial acetic acid (CH_3COOH), CAN dissociates into primarily $Ce(NO_3)_4$ (Henshall, 1963). Additionally, ceric ions containing complexed hydroxyl (OH) or H_2O, CH_3COOH, or acetonitrile (CH_3CN) molecules are formed in aqueous, acetic acid, or CH_3CN media, respectively (Henshall, 1963; Glebov et al., 2021). Higher solution acidity and/or CAN concentration appears to promote the formation of $Ce(NO_3)_6^{2-}$(Wylie, 1951) and ceric nitrate dimers (Blaustein and Gryder, 1957; Demars et al., 2015). The following generalized mechanism was proposed by Glass and Martin (1970) to describe ceric nitrate photochemistry:

$$Ce^{(IV)} + h\nu \rightarrow Ce^{(III)} + NO_3, \quad (R1)$$

$$Ce^{(III)} + NO_3 \rightarrow Ce^{(IV)}, \quad (R2)$$

$$NO_3 + NO_3 \rightarrow N_2O_6, \quad (R3)$$

$$N_2O_6 + 2Ce^{(IV)} \rightarrow 2NO_2 + O_2 + 2Ce^{(III)}, \quad (R4)$$

$$NO_3 + NO_2 + H_2O \rightarrow 2HNO_3, \quad (R5)$$

where $Ce^{(IV)}$ represents ceric nitrates as diverse as $Ce(NO_3)_4$, $Ce(NO_3)_6^{2-}$, $(NO_3)_5CeOCe(NO_3)_5^{4-}$, and $(H_2O)_3(NO_3)_3CeOCe(NO_3)_3(H_2O)_3$ that are potentially formed in solution (Blaustein and Gryder, 1957; Henshall, 1963; Demars et al., 2015). Similarly, $Ce^{(III)}$ represents cerous nitrates such as $Ce(NO_3)_3$ and $Ce(NO_3)_5^{2-}$. The rate of Reaction (R2) is [HNO_3]-dependent (Martin and Glass, 1970), and the dinitrogen hexaoxide (N_2O_6) intermediate was proposed on the basis of supporting observations without direct measurements (Glass and Martin, 1970).

CAN is used routinely as an oxidizing agent in organic synthesis due to its widespread availability, low cost, high oxidative potential, and low toxicity (Nair and Deepthi, 2007). However, its usage in atmospheric chemistry to date is limited to studies of NO_3-initiated oxidative aging processes in solution; e.g., Alexander (2004). Given the potential simplicity of irradiating $Ce^{(IV)}$ mixtures relative to synthesizing and storing N_2O_5 under cold and dry conditions or reacting $NO_2 + O_3$ under carefully controlled conditions, $Ce^{(IV)}$ irradiation could in principle enable more widespread studies of NO_3 oxidation chemistry, which is understudied compared to OH chemistry (Ng et al., 2017). Here, for the first time, we investigated the use of $Ce^{(IV)}$ irradiation as a source of gas-phase NO_3. First, we designed a photoreactor that generates gas-phase NO_3 from irradiated CAN / HNO_3 and CAN / $NaNO_3$ mixtures. Second, we characterized NO_3 concentrations achieved over a range of reactor operating conditions and mixture composition. Third, we characterized gas-phase reactive nitrogen and reactive oxygen species generated following $Ce^{(IV)}$ irradiation. Fourth, we demonstrated application of the method to generate and characterize oxygenated volatile organic compounds (OVOCs) and secondary organic aerosol (SOA) from the β-pinene + NO_3 reaction.

2 Methods

2.1 Photoreactor design and operation

Figure 1 shows a schematic of the experimental setup used in this study. A zero-air carrier gas flow of 0.5 L min^{-1} was bubbled through a gas dispersion line consisting of 6.35 mm o.d. × 4.8 mm i.d. fluorinated ethylene propylene (FEP) tubing into approximately 10 mL of aqueous CAN / HNO_3 or CAN / $NaNO_3$ mixtures placed at the bottom of a 12.7 mm o.d. × 11.1 cm i.d. FEP tube. The FEP tube was surrounded by low-pressure mercury fluorescent lamps installed vertically in a custom enclosure. These lamps had a 35.6 cm illuminated length. At these operating conditions, the calculated gas transit time in the illuminated portion of the reactor was approximately 3 s. After exiting the photoreactor, the carrier gas flow was passed through a filter holder (Savillex, 401-21-47-10-21-2) containing a 47 mm PTFE membrane filter (Pall Gelman, R2PJ047) to transmit NO_3 (Wagner et al., 2011) while removing stray droplets from the sample flow. At the end of each experiment, the lamps were turned off, the gas dispersion line was removed from the top of the reactor, and the FEP tubing and filter holder were flushed with distilled H_2O to remove residual $Ce^{(III)}$ precipitate. Initial studies were conducted using a cavity-attenuated phase-shift (CAPS) NO_2 monitor operating at $\lambda = 405$ nm (Kebabian et al., 2005) and a second retrofitted CAPS monitor operating at $\lambda = 630$ nm, which established that NO_2 and NO_3 were produced from irradiated $Ce^{(IV)}$. Subsequent studies

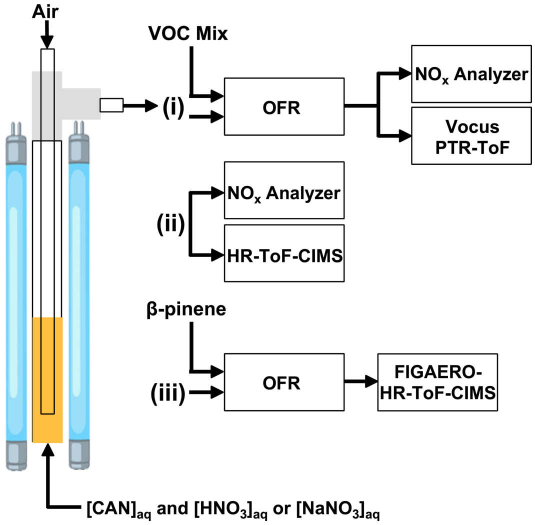

Figure 1. Overview of experiments conducted in this study. Aqueous mixtures of ceric ammonium nitrate (CAN) and nitric acid (HNO_3) or sodium nitrate ($NaNO_3$) were irradiated in a photoreactor to generate nitrate radicals (NO_3) in solution. Air was bubbled through the solution to evaporate NO_3 and other volatile photolysis products into the gas phase. The photoreactor effluent was then (i) injected into a dark oxidation flow reactor (OFR) along with a VOC mixture to characterize $[NO_3]$ via tracer decay measurements using a Vocus proton transfer reaction time-of-flight mass spectrometer (PTR-ToF) (ii) sampled with an iodide-adduct high-resolution time-of-flight chemical ionization mass spectrometer (HR-ToF-CIMS) (iii) injected into a dark OFR to characterize β-pinene / NO_3 oxidation products with a Filter Inlet for Gases and AEROsols (FIGAERO) coupled to the HR-ToF-CIMS. Supporting measurements were obtained using a NO_x analyzer.

described in the next section used a 2B Technologies model 405 analyzer to measure NO and NO_2 (Birks et al., 2018).

Depending on the specific experiment, lamps with peak emission output centered at $\lambda = 254$, 313, 369, or 421 nm, respectively (GPH436TL/4P, Light Sources, Inc.; F436T5/NBUVB/4P-313, F436T5/BLC/4P-369, F436T5/SDI/4P-421, LCD Lighting, Inc.) were used. Emission spectra from the manufacturer are shown in Fig. S1 in the Supplement. A fluorescent dimming ballast (IZT-2S28-D, Advance Transformer Co.) was used to regulate current applied to the lamps. To quantify the photon flux I_λ in the photoreactor for studies that used $\lambda = 254$, 313, or 369 nm radiation, we measured the rate of externally added O_3 ($\lambda = 254$ nm) or NO_2 photolysis ($\lambda = 313$ or 369 nm) as a function of lamp voltage under dry conditions (RH < 5 %). The photon flux was not quantified in studies that used $\lambda = 421$ nm radiation. NO_2 photolysis measurements were conducted in the absence of oxygen to avoid O_3 formation. Photon flux values were then calculated using methods described in Lambe et al. (2019); maximum values of $I_{254} = 1.0 \times 10^{16}$ photons cm^{-2} s^{-1}, $I_{313} = 6.0 \times 10^{15}$ photons cm^{-2} s^{-1}, and $I_{369} = 7.0 \times 10^{15}$ photons cm^{-2} s^{-1} were obtained.

2.2 Characterization studies

In one set of experiments, the 0.5 L min^{-1} photoreactor effluent was mixed with a 6.5 L min^{-1} zero-air carrier gas and injected into a dark Potential Aerosol Mass oxidation flow reactor (OFR; Aerodyne Research, Inc.), which is a horizontal 13 L conductive Teflon-coated aluminum cylindrical chamber operated in continuous flow mode. Approximately 6.5 L min^{-1} of sample flow was pulled from the reactor, resulting in a calculated mean residence time in the OFR (τ_{OFR}) of approximately 120 s. To constrain NO_3 mixing ratios, a mixture of 10 VOC tracers with NO_3 reaction rate coefficients (k_{NO_3}) ranging from 3.01×10^{-19} to 2.69×10^{-11} cm^3 molec.$^{-1}$ s^{-1} at $T = 298$ K (Table S1) was injected through a 10.2 cm length of 0.0152 cm i.d. Teflon tubing at a liquid flow rate of 0.94 µL h^{-1} using a syringe pump. The tracer mixture was then evaporated into a 1 L min^{-1} zero-air carrier gas prior to injection into the OFR. The total external NO_3 reactivity (NO_3R_{ext}), which is the summed product of each tracer mixing ratio and its k_{NO_3}, was approximately 5 s^{-1}. VOCs with proton affinities greater than that of H_2O were chosen to enable their measurement with a Tofwerk–Aerodyne Vocus proton transfer reaction time-of-flight mass spectrometer (hereafter referred to as "Vocus PTR") operated using H_3O^+ reagent ion chemistry (Krechmer et al., 2018) and ~ 8000 (Th / Th) resolving power. NO_3 mixing ratios were calculated from the measured decrease in VOC mixing ratios using the Vocus PTR. Here, we assumed that the total concentration of reacted VOCs was equal to the concentration of NO_3 injected into the OFR. Because NO_3 may additionally react with organic peroxy radicals (RO_2) generated from VOC + NO_3 reactions as well as OVOCs, these calculated NO_3 concentrations represent lower limits. Modeling calculations suggest that the fractional consumption of NO_3 by RO_2 ranged from < 0.01 to 0.17 over the range of conditions that were studied (Fig. S2). A subset of OVOCs generated from VOC + NO_3 reactions that had proton affinities greater than that of H_2O were also detected with the Vocus PTR.

In a separate set of experiments, the photoreactor effluent was diluted into 4 L min^{-1} zero-air carrier gas and sampled with an Aerodyne iodide-adduct high-resolution time-of-flight chemical ionization mass spectrometer (HR-ToF-CIMS; hereafter referred to as "CIMS"; Bertram et al., 2011) and the NO_x analyzer. The CIMS was operated at a ~ 4000 (Th / Th) resolving power. Iodide-adduct reagent ion chemistry was used due to its high sensitivity and selectivity towards nitrogen oxides and multifunctional organic nitrates (Lee et al., 2014). To demonstrate application of the method to study NO_3-initiated oxidative aging processes, the chemical composition of β-pinene + NO_3 gas- and condensed-phase oxidation products was measured with a Filter Inlet for Gases and AEROsols (FIGAERO) coupled to the CIMS (Lopez-Hilfiker et al., 2014). Gas sampling and simultaneous particle collection were performed for 1 min intervals, followed by thermal desorption of the particle sample from a PTFE filter membrane (15 min ramp from room temperature to 200 °C, 10 min holding time, 8 min cooldown to room temperature).

2.3 Photochemical model

To supplement our measurements, and to characterize aqueous-phase concentrations of species produced in the photoreactor that were not measured, we developed a photochemical box model that was implemented in the KinSim chemical kinetic solver (Peng and Jimenez, 2019). The KinSim mechanism shown in Table S2 contains reactions to model concentrations of $Ce^{(IV)}$, $Ce^{(III)}$, NO, NO_2, NO_3, N_2O_3, N_2O_4, N_2O_5, HNO_2, HNO_3, HNO_4, H, O, OH, HO_2, and H_2O_2. We assumed that HNO_3 that was present in solution prior to irradiation completely dissociated into H^+ and NO_3^-. When possible, we used condensed-phase rate coefficients in the mechanism. For reactions that we assumed occurred but did not have published condensed-phase rate coefficients (e.g., $NO_3 + OH \rightarrow NO_2 + HO_2$), we used published gas-phase rate coefficients instead with no modifications aside from unit conversion. Gas-phase wall loss rates of NO_x, NO_y, and HO_x species were not explicitly considered in the mechanism. UV–Vis extinction cross sections (σ_{ext}) of CAN / HNO_3 and CAN / $NaNO_3$ mixtures were separately obtained between $\lambda = 200$ and 600 nm using an Agilent Cary 5000 UV–Vis–NIR spectrophotometer. Because of the high absorptivity and concentrations of the mixtures, samples were prepared in a 0.01 mm short-path-length cuvette (20/C-Q-0.01, Starna) to minimize saturation of the photodetector relative to a cuvette with a standard 10 mm path length. Even with the cuvette that was used, CAN dilution was necessary in some cases in order to obtain σ_{ext} without photodetector saturation at shorter wavelengths. Spectra were obtained as a function of [CAN] (0.047 to 0.526 M), [HNO_3] (0 to 6.0 M), and [$NaNO_3$] (0 to 4.0 M) to cover the approximate range of mixture compositions that were characterized in Sect. 2.2. The σ_{ext} values of the mixture were then calculated using the Beer–Lambert law and applied in the KinSim mechanism. Model outputs were obtained over a total experimental time of 14400 s at 1 s intervals.

3 Results and discussion

The maximum NO_3 quantum yield (ϕ_{NO_3}) of UVA-irradiated CAN / HNO_3 mixtures is obtained at 6.0 M HNO_3 (Martin and Stevens, 1978); thus, this mixture composition served as the basis from which additional characterization studies were conducted. We found that 0.5 M CAN was the approximate solubility limit in 6.0 M HNO_3 at 25 °C. Because 1.1 M CAN is the solubility limit in H_2O and CAN is nearly insoluble in HNO_3 (Martin and Glass, 1970), 0.7 M CAN is the estimated solubility limit in 6.0 M HNO_3 in the absence of changes in ceric nitrate composition in solution. Thus, the reduction in CAN solubility (0.7 M → 0.5 M) observed in our studies was presumably associated with significant conversion of CAN to dimeric ceric nitrates in 6.0 M HNO_3 (Blaustein and Gryder, 1957; Demars et al., 2015).

3.1 NO_3 characterization studies

Figure 2a shows time series of thiophene (C_4H_4S), 2,3-dihydrobenzofuran (C_8H_8O), *cis*-3-hexenyl acetate ($C_8H_{14}O_2$), isoprene (C_5H_8), dimethyl sulfide (C_2H_6S), 2,5-dimethylthiophene (C_6H_8S), α-pinene ($C_{10}H_{16}$), and guaiacol ($C_7H_8O_2$) concentrations following injection into the OFR and exposure to NO_3 generated in the photoreactor from irradiation of a mixture of 0.5 M CAN and 6.0 M HNO_3 at $I_{369} = 7 \times 10^{15}$ photons $cm^{-2}\,s^{-1}$. Here, concentrations of each VOC were first normalized to the acetonitrile concentration to correct for changes in the syringe pump output over time and then normalized to the VOC concentration prior to NO_3 exposure. Aside from C_6H_8S, whose relative decay was less pronounced than expected (Table S1), and butanal (C_4H_8O, not shown), whose signal decreased by approximately 30 % and did not recover for reasons that are unclear, the oxidative loss of each tracer increased with increasing k_{NO_3}. Maximum tracer consumption was observed at the beginning of the experiment due to maximum NO_3 production from $Ce^{(IV)}$ irradiation. As the experiment progressed and $Ce^{(IV)}$ was reduced to $Ce^{(III)}$, the NO_3 concentration and corresponding VOC oxidative loss decreased. Compared to the other VOCs, the initial increase in $C_{10}H_{16}$ and $C_7H_8O_2$ concentrations over the first 2 h was delayed because of their higher k_{NO_3} values that resulted in > 95 % consumption and lower sensitivity to changes in [NO_3] in the initial stage of the experiment. To confirm that VOC degradation shown in Fig. 2a was due to reaction with NO_3, Fig. S3 shows the relative NO_3 rate coefficients obtained from the decay of C_4H_4S, C_8H_8O, and $C_8H_{14}O_2$ measured with the Vocus PTR. We measured relative rate coefficients of 3.59 between C_8H_8O and C_4H_4S and 6.92 between $C_8H_{14}O_2$ and C_4H_4S, which are in agreement with relative rate coefficient values of 3.44 ± 1.20 and 7.68 ± 2.84 calculated from their absolute NO_3 rate coefficients (Atkinson, 1991; D'Anna et al., 2001). Time series of ions corresponding to nitrothiophene ($C_4H_3NO_2S$), $C_5H_7NO_{4\text{–}6}$ and $C_{10}H_{15}NO_{5,6}$ organic nitrates, and nitroguaiacol ($C_7H_7NO_4$), which are known NO_3 oxidation products of C_4H_4S, C_5H_8, $C_{10}H_{16}$, and $C_7H_8O_2$ (Atkinson et al., 1990; Jenkin et al., 2003; Saunders et al., 2003; Cabañas et al., 2005), along with $C_8H_{5,7}NO_{4\text{–}6}$ and $C_8H_{13}NO_{5\text{–}6}$ ions that may be associated with NO_3 oxidation products of C_8H_8O and $C_8H_{14}O_2$, respectively, were anticorrelated with those of their respective VOC precursors (Fig. S4). Tracer decay experiments, similar to

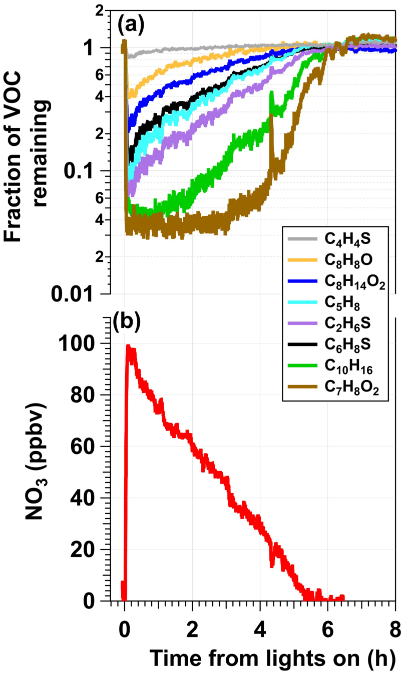

Figure 2. Example results from an experiment in which a mixture of 0.5 M CAN and 6.0 M HNO_3 was irradiated to generate NO_3 ($\lambda_{max} = 369$ nm, $I_{369} = 7 \times 10^{15}$ photons cm^{-2} s^{-1}) that was injected into the OFR along with a reactive VOC tracer mixture. **(a)** Time series of the fractional consumption of VOC tracers measured with the Vocus following irradiation: thiophene (C_4H_4S), 2,3-dihydrobenzofuran (C_8H_8O), *cis*-3-hexenyl-1-acetate ($C_8H_{14}O_2$), isoprene (C_5H_8), dimethyl sulfide (C_2H_6S), 2,5-dimethylthiophene (C_6H_8S), α-pinene ($C_{10}H_{16}$), and guaiacol ($C_7H_8O_2$). Signals of each tracer were normalized to their initial concentrations prior to NO_3 exposure and to acetonitrile concentrations to account for changes in the syringe pump output. **(b)** Time series of [NO_3] calculated from **(a)** and Table S1.

the one shown in Fig. S3, were used to obtain results that are discussed in more detail in Sect. 3.2, 3.3, and 3.4.

3.2 Effect of irradiation wavelength

Figure 3a shows normalized [NO_3] values obtained following irradiation of mixtures containing CAN and 6.0 M HNO_3 or 4.8 M $NaNO_3$ as a function of irradiation wavelength. In CAN / HNO_3 mixtures, [NO_3] was a factor of 2.4–3.5 higher following irradiation at $\lambda = 369$ compared to the other wavelengths. On the other hand, [NO_3] decreased with increasing irradiation wavelength following irradiation of CAN / $NaNO_3$ mixtures; at $\lambda = 254$ nm, [NO_3] was 3.2–42 times higher than at the other irradiation wavelengths that were used. These differences in [NO_3] were larger than the differences in calibrated photon flux values at the maximum output of each lamp type (±40 %; Sect. 2.1). Different $Ce^{(IV)}$ in CAN / HNO_3 and CAN / $NaNO_3$ mixtures may have influenced these trends, as suggested by their UV–Vis spectra (Fig. 3b). The σ_{ext} curves of CAN / HNO_3 mixtures were generally larger, broader, and redshifted relative to those of CAN / $NaNO_3$ mixtures, with the extent of red shifting increasing with larger [HNO_3], possibly due to higher yields of $Ce(NO_3)_6^{2-}$ and/or ceric nitrate dimers (Blaustein and Gryder, 1957; Henshall, 1963; Demars et al., 2015). For $\lambda > 250$ nm, CAN / HNO_3 mixtures had $\sigma_{ext,max}$ values between $\lambda = 306$–311 nm, whereas CAN / $NaNO_3$ solutions had $\sigma_{ext,max}$ values at $\lambda = 296$ nm. However, if [NO_3] was simply proportional to σ_{ext}, irradiation of CAN / HNO_3 mixtures at $\lambda = 313$ nm should have produced the highest [NO_3]; this was not the case. Instead, model calculations suggest that higher [NO_2] obtained from significantly faster photolysis of HNO_3 at $\lambda = 254$ and 313 nm relative to $\lambda > 350$ nm suppressed NO_3 downstream of the photoreactor when shorter irradiation wavelengths were used (Sander et al., 2011, Table S2). At a photon flux of 10^{16} photons cm^{-2} s^{-1}, model-calculated [NO_3] values were within ±13 % of each other for irradiation wavelengths ranging from $\lambda = 254$ to 369 nm. However, higher [NO_2] values obtained following $Ce^{(IV)}$ irradiation at $\lambda = 254$ and 313 nm suppressed NO_3 by > 96 % relative to the $\lambda = 369$ nm case during 120 s of simulated $NO_2 + NO_3$ reactions in the OFR. Thus, although the measured NO_3 suppression at these other irradiation wavelengths was less substantial than the model output, the measurement and model trends, along with achievement of maximum [NO_3] following $\lambda = 254$ nm irradiation of CAN / $NaNO_3$ mixtures that had lower [HNO_3], qualitatively support this explanation for the wavelength-dependent NO_3 yields observed in CAN / HNO_3 mixtures.

3.3 Effect of mixture composition

To characterize the influence of individual reagents on NO_3 formation, tracer decay experiments similar to the measurements shown in Fig. 2 were repeated as a function of [CAN], [HNO_3], and [$NaNO_3$]. Figure 4a shows [NO_3] obtained from irradiated 6.0 M HNO_3 solutions containing 0.001 to 0.5 M CAN ($I_{369} = 7 \times 10^{15}$ photons cm^{-2} s^{-1}) and irradiated 1.0 M $NaNO_3$ solutions containing 0.5 to 1.0 M CAN ($I_{254} = 1 \times 10^{16}$ photons cm^{-2} s^{-1}). Results were normalized to [NO_3] achieved with solutions containing 0.5 M CAN and 6.0 M HNO_3. Control experiments conducted with irradiated 6.0 M HNO_3 or 1.0 M $NaNO_3$ solutions at $I_{254} = 1 \times 10^{16}$ photons cm^{-2} s^{-1} in the absence of CAN suggest that a fraction of the NO_3 obtained in CAN mixtures was generated via the reactions $HNO_3 + h\nu \rightarrow OH + NO_2$ and $HNO_3 + OH \rightarrow NO_3 + H_2O$. The remaining NO_3 was clearly obtained from CAN irradiation because [NO_3] increased with increasing [CAN], as expected from Reaction (R1). Overall, [NO_3] increased by approximately a factor of 3 as [CAN] was increased from 0.001 to 0.5 M in 6.0 M HNO_3.

Figure 4b shows [NO_3] obtained in irradiated solutions containing 0.5 M CAN as a function of [HNO_3] ranging from

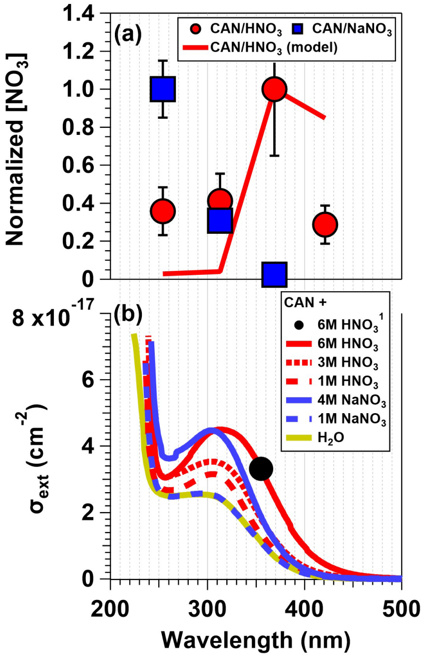

Figure 3. **(a)** $[NO_3]$ values obtained from irradiated CAN and 6.0 M HNO_3 and CAN and 4.8 M $NaNO_3$ mixtures as a function of irradiation wavelengths. Results were normalized to $[NO_3]$ achieved with irradiation of CAN / HNO_3 mixtures at $\lambda = 369$ nm or CAN / $NaNO_3$ mixtures at $\lambda = 254$ nm. Error bars represent $\pm 1\sigma$ uncertainty in binned $[NO_3]$ values. **(b)** Extinction cross sections (σ_{ext}) of CAN / HNO_3 and CAN / $NaNO_3$ mixtures (for details see Sect. 2.3). The black dot (note the superscripted 1 in the legend) corresponds to data from Wine et al. (1988).

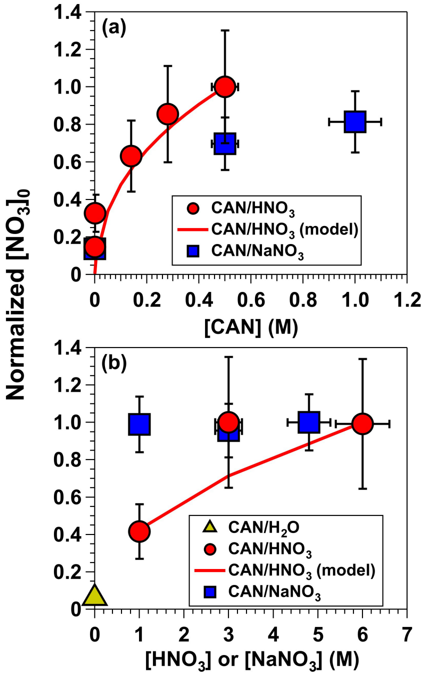

Figure 4. $[NO_3]$ obtained from **(a)** irradiated 6.0 M HNO_3 solutions containing 0.001 to 0.5 M CAN ($I_{369} = 7 \times 10^{15}$ photons $cm^{-2}\,s^{-1}$), and irradiated 1.0 M $NaNO_3$ solutions containing 0.5 to 1.0 M CAN ($I_{254} = 1 \times 10^{16}$ photons $cm^{-2}\,s^{-1}$). **(b)** Irradiated 0.5 M CAN solutions containing 1.0 to 6.0 M $[HNO_3]$ or 1.0 to 4.8 M $[NaNO_3]$ at the same I_{369} and I_{254} values used to obtain results shown in **(a)**. Results were normalized to $[NO_3]$ achieved with mixtures of 0.5 M CAN and 6.0 M HNO_3. Error bars represent estimated ±35 % uncertainty in $[NO_3]$ values obtained from CAN / HNO_3 mixtures; ±15 % uncertainty in $[NO_3]$ values obtained from CAN / $NaNO_3$ mixtures; and ±10 % uncertainty in [CAN], $[HNO_3]$, and $[NaNO_3]$ values.

1.0 to 6.0 M or $[NaNO_3]$ ranging from 1.0 to 4.8 M at the same I_{369} and I_{254} values used to obtain results shown in Fig. 4a. Irradiated CAN solutions containing 3.0 and 6.0 M HNO_3 generated the same $[NO_3]$ concentrations within measurement uncertainties, presumably because the NO_3 quantum yield (ϕ_{NO_3}) ranged from 0.92–1.00 over this range of acidity (Martin and Stevens, 1978; Wine et al., 1988). $[NO_3]$ decreased by a factor of 2 as $[HNO_3]$ was decreased from 3.0 to 1.0 M, consistent with a reduction in ϕ_{NO_3} from 0.92 to 0.46 (Martin and Stevens, 1978). On the other hand, in irradiated CAN / $NaNO_3$ mixtures with uncharacterized ϕ_{NO_3}, $[NO_3]$ was constant within measurement uncertainties between 1.0 and 4.8 M $NaNO_3$.

Other mixture components that were tested or considered included substitution of CH_3CN in place of H_2O and HNO_3, ammonium nitrate (NH_4NO_3) instead of $NaNO_3$, ceric potassium nitrate ($K_2Ce(NO_3)_6$) instead of CAN, and addition of sodium persulfate ($Na_2S_2O_8$) to generate additional NO_3 via $S_2O_8^{2-} + h\nu \rightarrow 2SO_4^-$ followed by $SO_4^- + NO_3^- \rightarrow NO_3 + SO_4^{2-}$ (Gaillard de Sémainville et al., 2007). CAN / CH_3CN mixtures are commonly used in organic synthesis applications, perhaps even more so than CAN / HNO_3 (Baciocchi et al., 1988; Choidini et al., 1993; Alexander, 2004). In limited testing, CAN / CH_3CN appeared to generate significantly less NO_3 than CAN / HNO_3 or CAN / $NaNO_3$, possibly due to lower ϕ_{NO_3} of irradiated $Ce^{(IV)}$–CH_3CN complexes (Glebov et al., 2021) and/or suppression of NO_3 due to its reaction with CH_3CN in solution. $K_2Ce(NO_3)_6$ is less widely available and less water soluble than CAN and therefore was not considered further. Irradiation of CAN / NH_4NO_3 and CAN / $NaNO_3$ mixtures generated similar $[NO_3]$, but we prefer $NaNO_3$ due to its lower volatility. Finally, ternary mixtures containing 0.5 M CAN + 2.0 M $NaNO_3$ + 0.5 M $Na_2S_2O_8$ irradiated at $\lambda = 254$ nm generated negligible additional NO_3 compared to binary CAN / $NaNO_3$ mixtures.

3.4 Effect of photon flux

Figure 5 shows normalized $[NO_3]$ values obtained from irradiated mixtures of (1) 0.5 M CAN and 6.0 M HNO_3 ($\lambda = 369$ nm) and (2) 0.5 M CAN and 1.0 M $NaNO_3$

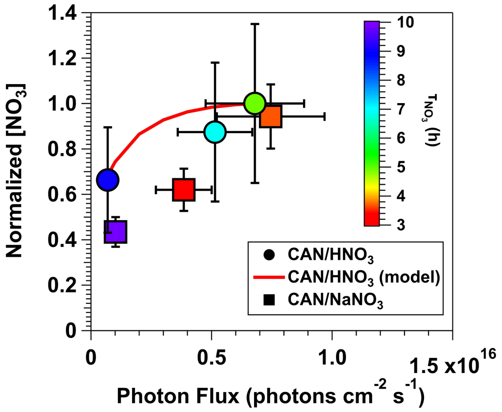

Figure 5. Normalized [NO_3] values obtained from irradiated mixtures of 0.5 M CAN and 6.0 M HNO_3 ($\lambda = 369$ nm) or 0.5 M CAN and 1.0 M $NaNO_3$ ($\lambda = 254$ nm) as a function of photon flux ranging from 6.9×10^{14} to 7.5×10^{15} photons cm^{-2} s^{-1}. Results were normalized to [NO_3] achieved with 0.5 M CAN, 6.0 M HNO_3, and $I_{369} = 6.8 \times 10^{15}$ photons cm^{-2} s^{-1}. Symbols are colored by the time it took for [NO_3] to experience one *e*-folding decay relative to the maximum [NO_3] that was measured (τ_{NO_3}). Error bars represent estimated ±35 % uncertainty in [NO_3] values obtained from CAN / HNO_3 mixtures, ±15 % uncertainty in [NO_3] values obtained from CAN / $NaNO_3$ mixtures, and ±30 % uncertainty in photon flux values.

($\lambda = 254$ nm) as a function of photon flux ranging from 6.9×10^{14} to 7.5×10^{15} photons cm^{-2} s^{-1}. Results for both CAN / HNO_3 and CAN / $NaNO_3$ mixtures were normalized to [NO_3] achieved with 0.5 M CAN, 6.0 M HNO_3, and $I_{369} = 6.8 \times 10^{15}$ photons cm^{-2} s^{-1}. Symbols are colored by the NO_3 lifetime (τ_{NO_3}), defined here as the time it took for [NO_3] to experience one *e*-folding decay relative to the maximum [NO_3] that was measured. Figure 5 shows that [NO_3] increased with increasing photon flux, consistent with the fact that it is a primary photolysis product, along with a concurrent decrease in τ_{NO_3} due to faster reduction of Ce$^{(IV)}$ to Ce$^{(III)}$. For the CAN / HNO_3 system, [NO_3] increased by a factor of 1.5 as I_{369} was increased from 6.9×10^{14} to 6.8×10^{15} photons cm^{-2} s^{-1}, in agreement with the model-calculated increase in [NO_3] within measurement uncertainty. τ_{NO_3} decreased from 9 to 5 h. For the CAN / $NaNO_3$ system, [NO_3] increased by a factor of 1.9 as I_{254} was increased from 1.0×10^{15} to 7.5×10^{15} photons cm^{-2} s^{-1}, and τ_{NO_3} decreased from 10 to 3 h.

To examine concentrations of NO_3 and a subset of additional gas-phase photolysis products obtained over a wider range of conditions, Fig. 6 plots model-calculated [NO_3], $NO_2 : NO_3$, $HO_2 : NO_3$, and $N_2O_5 : NO_3$ values as a function of photon flux ranging from 1×10^{14} to 1×10^{17} photons cm^{-2} s^{-1} following $\lambda = 254$, 313, 369, and 421 nm irradiation of a mixture of 0.5 M CAN and 6.0 M HNO_3. Figure 6a also plots the measured [NO_3] obtained from irradiation of a mixture of 0.5 M CAN and 6.0 M HNO_3 at $I_{369} = 7 \times 10^{15}$ photons cm^{-2} s^{-1} (Fig. 2) after correcting for dilution between the photoreactor and the OFR (Sect. 2.2) as well as application of a NO_3 wall loss rate coefficient of 0.2 s^{-1} within the photoreactor (Dubé et al., 2006). At this photon flux value, the model-calculated [NO_3] = 1.4 ppmv agrees with [NO_3] = 1.7 ± 0.6 ppmv obtained from measurements. When considering only the primary photochemical process (Reactions R1–R5), maximum [NO_3] values within ±10 % of each other were achieved at photon fluxes ranging from 5×10^{15} ($\lambda = 313$ nm) to 4×10^{16} photons cm^{-2} s^{-1} ($\lambda = 421$ nm). [NO_3] values decreased at higher photon flux values due to conversion of NO_3 to NO_2 via photolysis. As shown in Fig. 6b, significant additional NO_2 production was obtained via HNO_3 photolysis at shorter irradiation wavelengths above $I \approx 10^{15}$ photons cm^{-2} s^{-1}, resulting in $NO_2 : NO_3 > 10$ ($\lambda = 254$ nm) and 1 ($\lambda = 313$ nm). Given additional reaction time downstream of the photoreactor, high NO_2 may suppress NO_3 (Sect. 3.2) and increase $N_2O_5 : NO_3$ beyond the range of values shown in Fig. 6c. We also calculated OH : NO_3 and $HO_2 : NO_3$ following irradiation of CAN / HNO_3 mixtures over the range of conditions shown in Fig. 6. Aqueous OH : $NO_3 \approx 0.1$ and did not change significantly as a function of photon flux or irradiation wavelength, and aqueous $HO_2 : NO_3$ values ranged from 0.05 ($\lambda = 254$ nm) to 0.25 ($\lambda \geq 369$ nm). While OH influenced aqueous-phase chemistry inside the photoreactor via formation of reactive oxygen species (Sect. 3.5), OH probably did not influence downstream gas-phase chemistry due to significant wall losses inside the photoreactor: assuming a lower-limit OH wall loss rate coefficient of 5 s^{-1} (Schwab et al., 1989), the estimated OH penetration efficiency through the reactor was less than 10^{-6}.

3.5 Characterization of reactive nitrogen and reactive oxygen photolysis products

Figure 7 shows time series of reactive nitrogen and reactive oxygen species detected following irradiation of the same mixture of 0.5 M CAN and 1.0 M $NaNO_3$ ($I_{254} \approx 10^{16}$ photons cm^{-2} s^{-1}), shown here because the signal-to-noise ratio in CIMS measurements of irradiated CAN / $NaNO_3$ mixtures was generally better than in measurements of irradiated CAN / HNO_3 mixtures due to reagent ion depletion by HNO_3. A time series of [NO_3] obtained separately from VOC tracer decay measurements under similar irradiation conditions is also shown. The NO_2 and NO_3 mixing ratios reached maximum values of 26 and 58 ppbv shortly after the lights were turned on (Fig. 7a), suggesting an initial $NO_2 : NO_3 \approx 0.45$ (Fig. 4). Multiple reactions may generate NO_2, including Reaction (R3), HNO_3 photolysis, and/or NO_3 photolysis as well as other reactions listed in Table S2. While NO_2 and/or HNO_2 photolysis generated NO, its concentration was negligible in these experiments.

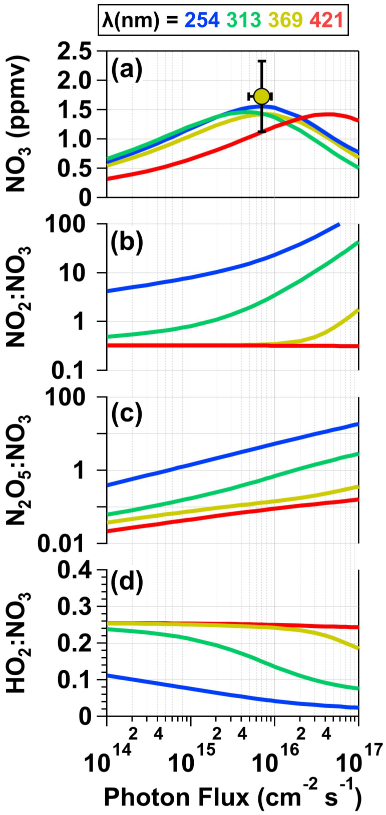

Figure 6. Model-calculated **(a)** [NO_3], **(b)** $NO_2 : NO_3$, **(c)** $HO_2 : NO_3$, and **(d)** $N_2O_5 : NO_3$ values in solution as a function of photon flux ranging from 1×10^{14} to 1×10^{17} photons cm^{-2} s^{-1} following $\lambda = 254$, 313, 369, and 421 nm irradiation of a mixture containing 0.5 M CAN and 6.0 M HNO_3. [NO_3] obtained from measurements shown in Fig. 2 is plotted in **(a)**. For details see Sect. 2.3 and Table S2.

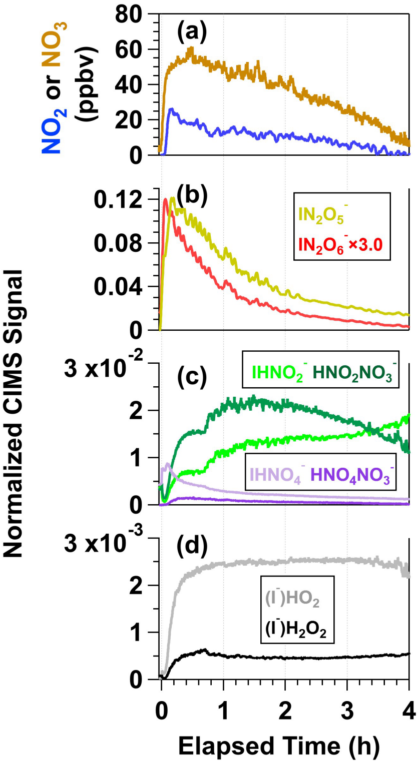

Figure 7. Time series of **(a)** NO_2 and NO_3, **(b)** N_2O_5 and N_2O_6, **(c)** HNO_2 and HNO_4, and **(d)** HO_2 and H_2O_2 detected following irradiation of a mixture containing 0.5 M CAN and 1.0 M $NaNO_3$. N_2O_5, N_2O_6, HO_2, and H_2O_2 were detected as I^- adducts, and HNO_2 and HNO_4 were detected as both I^- and NO_3^- adducts with HR-ToF-CIMS. CIMS signals detected as iodide adducts were normalized to the I^- signal prior to the start of the experiment, and CIMS signals detected as nitrate adducts were normalized to the maximum NO_3^- obtained during the experiment (see Fig. S5).

Figure 7b shows time series of $IN_2O_5^-$ and $IN_2O_6^-$ signals measured with the CIMS. $IN_2O_5^-$ was formed from $NO_2 + NO_3 \rightarrow N_2O_5$ reactions in the photoreactor and $N_2O_5 + I^- \rightarrow IN_2O_5^-$ reactions in the CIMS ion molecule reactor (IMR). As expected, $IN_2O_5^-$ followed a similar profile as NO_2 and NO_3. $IN_2O_6^-$ was either generated from $NO_3 + NO_3 \rightarrow N_2O_6$ reactions in the photoreactor (Glass and Martin, 1970) followed by $N_2O_6 + I^- \rightarrow IN_2O_6^-$ reactions in the IMR or from the following series of reactions in the IMR: $HNO_3 + IO^- \rightarrow NO_3^- + HOI$, $HOI + NO_3^- \rightarrow INO_3 + OH^-$, and $INO_3 + NO_3^- \rightarrow IN_2O_6^-$ (Ganske et al., 2019). To further explore the plausibility of N_2O_6 formation in this system, we conducted a theoretical investigation of the gas-phase $NO_3 + NO_3 \rightarrow N_2O_6$ reaction and found that this reaction is exothermic, even more so than $NO_3 + NO_3 \rightarrow N_2O_5$. Additional details regarding this analysis are provided in Sect. S1.

Figure 7c shows time series of $IHNO_2^-$, $HNO_2NO_3^-$, $IHNO_4^-$, and $HNO_4NO_3^-$. These ions are associated with nitrous acid (HNO_2) and peroxynitric acid (HNO_4), respectively (Veres et al., 2015). Because rapid formation of $HNO_{2-4}NO_3^-$ ions was observed following $Ce^{(IV)}$ irradiation, and because IO_x^- signals were relatively low (Sect. S2.1), we hypothesize that $I^- +$ NO_3 and/or $I^- + HNO_3$ reactions were the main source of NO_3^- (Lee et al., 2014; Dörich et al., 2021) and that subsequent competitive $NO_3^- + HNO_{2-4}$ and $I^- + HNO_{2-4}$ reactions in the IMR generated both $IHNO_{2-4}^-$ and $HNO_{2-4}NO_3^-$. HNO_4 was generated following the reactions $HNO_3 + h\nu \rightarrow OH + NO_2$, $OH + NO_3 \rightarrow HO_2 + NO_2$, and $HO_2 + NO_2 \rightarrow HNO_4$. This hypothesis is supported by the similarity between NO_2 and $IHNO_4^-$ time series coupled with the relatively constant concentrations of HO_2 generated via $OH + OH \rightarrow H_2O_2$ and $OH + H_2O_2 \rightarrow HO_2 + H_2O$ reactions. H_2O_2, detected as $IH_2O_2^-$, also behaved similarly as IHO_2^- (Fig. 7d). HNO_2 had a different temporal profile than the other nitrogen oxides: $IHNO_2^-$ increased throughout the experiment, and $HNO_2NO_3^-$ increased and then decreased. We hypothesize that $NO_2 + NO_2 \rightarrow N_2O_4$ and

$N_2O_4 + H_2O \rightarrow HNO_2 + HNO_3$ reactions were the main source of HNO_2 (Sect. S2.2).

Figure S13 shows time series of the same ions plotted in Fig. 7 following irradiation of a solution containing 0.5 M CAN and 3.0 M HNO_3 ($I_{369} \approx 7 \times 10^{15}$ photons $cm^{-2}\,s^{-1}$). Here, 3.0 M HNO_3 was used because 6.0 M HNO_3 depleted the CIMS reagent ion too much ($IHNO_3^- : I^- \approx 15$) to achieve signal-to-noise ratio that was sufficient for comparison to CAN / $NaNO_3$ mixtures ($IHNO_3^- : I^- \approx 3$). The same gas-phase nitrogen oxides and reactive oxygen species were observed in this reaction system as with the irradiated CAN / $NaNO_3$ mixture. The relative yields of each compound plotted in Figs. 7 and S13 were within a factor of 3 of each other, although signals of nitrogen oxides and reactive oxygen species obtained from irradiated CAN / HNO_3 mixtures decreased at a slower rate than the same compounds obtained from irradiated CAN / $NaNO_3$ mixtures. These trends may be due to different $Ce^{(IV)}$ composition (Fig. 3 and Sect. 3.2) and/or an enhanced rate of $Ce^{(III)} + NO_3 \rightarrow Ce^{(IV)}$ reactions in HNO_3 relative to $NaNO_3$ (Reaction R2).

3.6 OVOC–SOA generation from β-pinene + NO_3

To demonstrate proof of principle for NO_3-initiated oxidative aging studies, we generated NO_3 via irradiation of a mixture of 0.5 M CAN and 3.0 M HNO_3 ($I_{369} = 7 \times 10^{15}$ photons $cm^{-2}\,s^{-1}$), reacted it with β-pinene in a dark OFR, and obtained FIGAERO-CIMS spectra of gas- and condensed-phase β-pinene + NO_3 oxidation products (Sect. 2.2). Figure 8a shows a spectrum of gas-phase β-pinene / NO_3 oxidation products detected between $m/Q = 320$ and 420, where the majority of the signal was observed; signals shown are unmodified $(M + I)^-$ formulas. The largest ion detected was at $m/Q = 356$ ($IC_{10}H_{15}NO_5^-$), which represents a major first-generation dicarbonyl nitrate oxidation product with a relative abundance of 0.31 and a calculated saturation vapor pressure of 2×10^{-7} atm ($C^* = 1900\,\mu g\,m^{-3}$; Claflin, 2018). Other ions corresponding to first-generation hydroxycarbonyl nitrate ($IC_{10}H_{17}NO_5^-$, $C^* = 95\,\mu g\,m^{-3}$), tricarbonyl nitrate ($IC_{10}H_{15}NO_6^-$, $C^* = 35\,\mu g\,m^{-3}$), hydroxydicarbonyl nitrate ($IC_{10}H_{17}NO_6^-$, $C^* = 4.7\,\mu g\,m^{-3}$), and hydroxycarbonyl nitrate acid ($IC_{10}H_{17}NO_7^-$, $C^* = 0.29\,\mu g\,m^{-3}$) products were detected in addition to $IC_9H_{13}NO_5^-$ and a suite of additional previously characterized C_8 and C_9 organic nitrates (Nah et al., 2016; Takeuchi and Ng, 2019; Shen et al., 2021). The $IC_{10}H_{16}N_2O_7^-$ hydroxy dinitrate, which was also previously observed in FIGAERO-CIMS spectra of α-pinene / NO_3 SOA (Nah et al., 2016), was generated via an unknown reaction pathway. Overall, the high molar yield and vapor pressure of $C_{10}H_{15}NO_5$ (Claflin, 2018) are consistent with it having the highest relative abundance in the gas phase (Fig. 8a), whereas the other C_{10} β-pinene oxidation products were semivolatile under our experimental conditions.

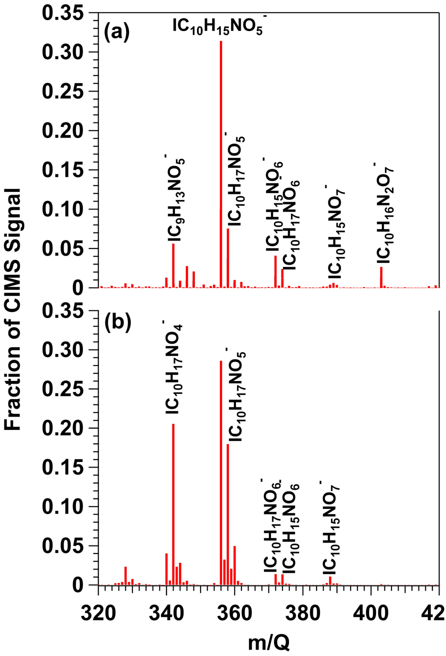

Figure 8. HR-ToF-CIMS spectra of gas-phase β-pinene / NO_3 oxidation products obtained following β-pinene reaction with NO_3 generated via **(a)** irradiation of a mixture of 0.5 M CAN and 3.0 M HNO_3 and subsequent injection into the OFR **(b)** thermal decomposition of N_2O_5 injected into the Georgia Tech environmental chamber. Signals shown are unmodified $(M + I)^-$ formulas.

Figure 9a shows a spectrum of condensed-phase β-pinene / NO_3 oxidation products obtained with the FIGAERO-CIMS; signals were averaged over the entire thermal desorption cycle and are plotted on logarithmic scale and represent unmodified $(M + I)^-$ formulas. To aid interpretation of the major features of the spectrum, bands of ion signals corresponding to $IC_{10}H_{15}NO_x^-$, $IC_{20}H_{32}N_2O_x^-$, and $IC_{30}H_{47}N_3O_x^-$ oxidation products were highlighted and colored by the number of oxygen atoms in their chemical formulas. Here, the largest ion detected was at $m/Q = 372$ ($IC_{10}H_{15}NO_6^-$), which is the condensed-phase component of the same tricarbonyl nitrate detected in the gas phase (Fig. 8a). $IC_{10}H_{15}NO_5^-$ and $IC_{10}H_{15}NO_{7-9}^-$ signals were also detected. The second-largest ion signal was measured at $m/Q = 571$ ($IC_{20}H_{32}N_2O_9^-$), an acetal dimer obtained from the condensed-phase reaction of two $C_{10}H_{17}NO_5$ monomers followed by H_2O elimination (Claflin and Ziemann, 2018). Similar accretion reactions between other C_{10} organic nitrates yielded $IC_{20}H_{32}N_2O_8^-$ and $IC_{20}H_{32}N_2O_{10-13}^-$ signals. Likewise, reactions between C_{10} monomers and C_{20} dimers generated C_{30} trimers detected between $m/Q = 768$–864 ($IC_{30}H_{47}N_3O_{12-18}^-$). The largest trimer-related ion, $IC_{30}H_{47}N_3O_{12}^-$, was generated from $C_{10}H_{17}NO_4 + C_{20}H_{32}NO_9 - H_2O$ or $C_{10}H_{17}NO_5 + C_{20}H_{32}NO_8 - H_2O$ reactions (Claflin and Ziemann, 2018). A fourth cluster of ion signals at

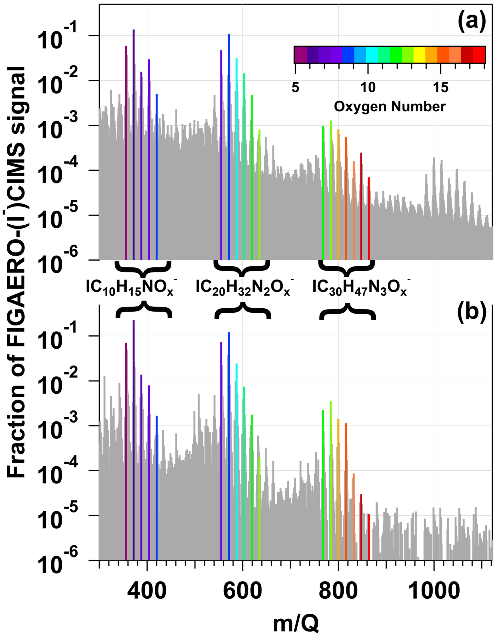

Figure 9. FIGAERO–HR-ToF-CIMS spectra of condensed-phase β-pinene / NO_3 oxidation products obtained following β-pinene reaction with NO_3 generated via **(a)** irradiation of a mixture of 0.5 M CAN and 3.0 M HNO_3 and subsequent injection into an OFR and **(b)** thermal decomposition of N_2O_5 injected into the Georgia Tech environmental chamber. Signals shown are unmodified $(M+I)^-$ formulas. Bands of ion signals corresponding to $C_{10}H_{15}NO_x$, $C_{20}H_{32}N_2O_x$, and $C_{30}H_{47}N_3O_x$ oxidation products are highlighted and colored by the number of oxygen atoms in their chemical formulas.

$m/Q > 984$ was also observed. Unambiguous assignment of chemical formulae to these signals was challenging due to the limited range of the CIMS m/z calibration and lack of available information about $C_{>30}$ β-pinene / NO_3 oxidation products. However, it seems plausible that these signals are associated with tetramers.

To compare our results with those obtained using a conventional NO_3 generation method (room-temperature N_2O_5 thermal decomposition) in an environmental chamber study, Figs. 8b and 9b show reference gas- and condensed-phase FIGAERO-I⁻-CIMS spectra of OVOCs and SOA generated from NO_3 oxidation of β-pinene in the Georgia Tech environmental chamber (Takeuchi and Ng, 2019). The spectra obtained here and by Takeuchi and Ng (2019) exhibit an overall high degree of similarity, with linear correlation coefficients of 0.87 and 0.96 between the respective gas- and condensed-phase spectra. Clusters of $IC_{10}H_{15}NO_x^-$, $IC_{20}H_{32}N_2O_x^-$, and $IC_{30}H_{47}N_3O_x^-$ ion signals are present in both Fig. 9a and b. The main differences between the gas-phase spectra shown in Figs. 8a and 9a were the different abundances of $IC_{10}H_{17}NO_4^-$, a first-generation hydroxynitrate product (Claflin and Ziemann, 2018), and $IC_{10}H_{16}N_2O_7^-$. Because $C_{10}H_{17}NO_4$ is formed from RO_2+RO_2 reactions (DeVault et al., 2022) and is sufficiently volatile ($C^* = 750\,\mu g\,m^{-3}$) to partition into the gas phase (Claflin, 2018), differences in gas-phase $C_{10}H_{17}NO_4$ and $C_{10}H_{16}N_2O_7$ yields were likely related to differences in the relative importance of RO_2+RO_2 versus RO_2+NO_3 reaction pathways in the study by Takeuchi and Ng (2019) compared to this work.

To further investigate the fate of RO_2 generated from VOC + NO_3 reactions as a function of CAN irradiation conditions, we calculated the fractional oxidative loss of generic alkyl and acyl RO_2 species due to reactions with HO_2, NO_3, and NO_2 ($F_{RO_2+HO_2}$, $F_{RO_2+NO_3}$, $F_{RO_2+NO_2}$) using Eqs. (1)–(3):

$$F_{RO_2+HO_2} = \frac{k_{RO_2+HO_2}[HO_2]}{k_{RO_2+HO_2}[HO_2]+k_{RO_2+NO_3}[NO_3]+k_{RO_2+NO_2}[NO_2]}, \quad (1)$$

$$F_{RO_2+NO_3} = \frac{k_{RO_2+NO_3}[NO_3]}{k_{RO_2+HO_2}[HO_2]+k_{RO_2+NO_3}[NO_3]+k_{RO_2+NO_2}[NO_2]}, \quad (2)$$

$$F_{RO_2+NO_2} = \frac{k_{RO_2+NO_2}[NO_2]}{k_{RO_2+HO_2}[HO_2]+k_{RO_2+NO_3}[NO_3]+k_{RO_2+NO_2}[NO_2]}. \quad (3)$$

Here, $k_{RO_2+HO_2}$, $k_{RO_2+NO_3}$, and $k_{RO_2+NO_2}$ are reaction rate coefficients for the corresponding RO_2+HO_2, RO_2+NO_3, and RO_2+NO_2 forward reactions whose values are summarized in Table S3. Several simplifying assumptions were made. First, we assumed that RO_2 + NO reactions were negligible. Second, we did not consider RO_2 isomerization–autoxidation and RO_2+RO_2 reactions that are influenced by external factors. Third, we set $F_{RO_2+NO_2}=0$ for alkyl-RO_2-generated RO_2NO_2, which thermally decomposes on timescales of seconds or less (Orlando and Tyndall, 2012). Fourth, we assumed that vapor wall losses of acyl-RO_2-generated RO_2NO_2 were a minor RO_2 sink because the OFR residence time ($\tau_{OFR} \approx 120$ s, Sect. 2.2) was significantly shorter than their estimated wall loss timescale ($\tau_{wall} \approx 400$ s; Palm et al., 2016). Figure 10 shows calculated $F_{RO_2+HO_2}$, $F_{RO_2+NO_3}$, and $F_{RO_2+NO_2}$ values for alkyl-RO_2 and acyl-RO_2 as a function of photon flux over the range of NO_3 generation conditions presented in Fig. 6. For alkyl-RO_2, $F_{RO_2+HO_2}$ decreased and $F_{RO_2+NO_3}$ increased with increasing photon flux and decreasing irradiation wavelength. On the other hand, for acyl-RO_2, $F_{RO_2+NO_2}$ increased, while $F_{RO_2+HO_2}$ and $F_{RO_2+NO_3}$ decreased over the same irradiation conditions. Overall, at the optimal NO_3 generation conditions (e.g., $\lambda = 369$ nm and $I_{369} \approx 10^{16}$ photons $cm^{-2}\,s^{-1}$), our calculations suggest that $F_{RO_2+HO_2} \approx F_{RO_2+NO_3}$ for alkyl-RO_2 (Fig. 10c) and that $F_{RO_2+HO_2} \approx F_{RO_2+NO_3} \approx F_{RO_2+NO_2}$ for acyl-RO_2 (Fig. 10g).

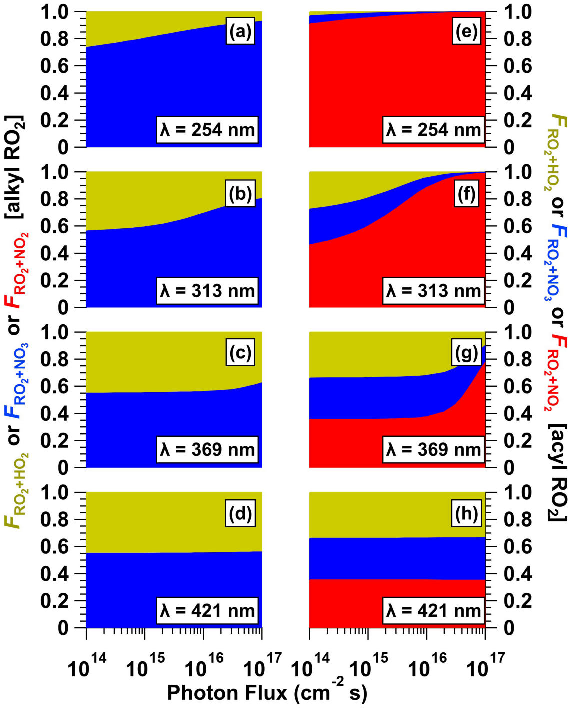

Figure 10. Fractional oxidative loss of alkyl and acyl organic peroxy radicals (RO_2) due to reaction with HO_2, NO_3, and NO_2 ($F_{RO_2+HO_2}$, $F_{RO_2+NO_3}$, and $F_{RO_2+NO_2}$) generated following **(a, e)** $\lambda = 254$, **(b, f)** $\lambda = 313$, **(c, g)** $\lambda = 369$, and **(d, h)** $\lambda = 421$ nm irradiation of a mixture containing 0.5 M CAN and 6.0 M HNO_3 as a function of photon flux ranging from 1×10^{14} to 1×10^{17} photons $cm^{-2}\,s^{-1}$.

4 Conclusions

$Ce^{(IV)}$ irradiation complements $NO_2 + O_3$ reactions and N_2O_5 thermal dissociation as a customizable photolytic NO_3 source. Important method parameters were [CAN], [HNO_3], or [$NaNO_3$]; UV intensity; and irradiation wavelength. By contrast, important parameters for $NO_2 + O_3$ and N_2O_5 based methods are [O_3], [NO_2], temperature, and humidity. Because $Ce^{(IV)}$ irradiation already generates NO_3 in aqueous solution, its performance is not hindered by humidity to the same extent (if at all) as N_2O_5-based methods, where hydrolysis of N_2O_5 to HNO_3 decreases the efficacy of the source. Additionally, the $NO_3 + H_2O$ reaction rate in solution or on surfaces is slow in relation to other NO_3 loss pathways (Jiang et al., 1992). Another advantage of $Ce^{(IV)}$ irradiation is that it does not involve the use of O_3 as a reagent; therefore it eliminates the possibility of competing O_3 and NO_3 oxidation of compounds that are reactive towards both oxidants if $NO_2 + O_3$ reactions and/or online N_2O_5 synthesis are used as the NO_3 source (Lambe et al., 2020). To identify optimal operating conditions for maximizing [NO_3], we characterized concentrations of NO_3 at [CAN] $= 10^{-3}$ to 1 M, [HNO_3] $= 1.0$ to 6.0 M, [$NaNO_3$] $= 1.0$ to 4.8 M, a photon flux of 6.9×10^{14} to 1.0×10^{16} photons $cm^{-2}\,s^{-1}$, and irradiation wavelengths of $\lambda = 254$, 313, 369, or 421 nm. With CAN / HNO_3 mixtures, maximum [NO_3] was achieved with [CAN] ≈ 0.5 M, [HNO_3] ≈ 3.0 to 6.0 M, and $I_{369} = 8 \times 10^{15}$ photons $cm^{-2}\,s^{-1}$ (4.3 mW cm^{-2}). With CAN / $NaNO_3$ mixtures, maximum [NO_3] was achieved with [CAN] ≈ 1.0 M, [$NaNO_3$] ≥ 1.0 M, and $I_{254} \approx 1 \times 10^{16}$ photons $cm^{-2}\,s^{-1}$ (7.8 mW cm^{-2}). Thus, for applications such as environmental chambers or OFR studies of NO_3-initiated oxidative aging processes, where significant NO_3 production over relatively short time periods is beneficial, irradiation of concentrated $Ce^{(IV)}$ solutions at high photon flux is advantageous. Other applications that require sustained NO_3 production at lower concentrations and/or over longer time periods may benefit from using lower [$Ce^{(IV)}$] and photon flux. Overall, because $Ce^{(IV)}$ irradiation generates NO_3 at room temperature using widely available, low-cost reagents and light sources (including high-power light-emitting diodes in addition to, or instead of, UV fluorescent lamps), it is easier to apply than other NO_3 generation techniques – especially in field studies – and it may therefore enable more widespread studies of NO_3 oxidation chemistry. Adapting a photoreactor to operate with continuous injection of fresh $Ce^{(IV)}$ or alternative photolytic NO_3 precursors (e.g., Hering et al., 2015) rather than in batch mode, as was done here, may further enhance its performance and will be investigated in future work.

Code and data availability. Data presented in this paper are available upon request. The KinSim mechanism used in this paper is included with the Supplement. The KinSim kinetic solver is freely available at https://gitlab.com/JimenezGroup/KinSim_Code (Peng and Jimenez, 2023).

Supplement. The supplement related to this article is available online at: https://doi.org/10.5194/acp-23-13869-2023-supplement.

Author contributions. ATL, BB, and PL conceived and planned the experiments. ATL, BB, MWA, and PL carried out the experiments. ATL conceived, planned, and carried out the KinSim model simulations. NO and PMZ conceived, planned, and carried out the quantum chemical calculations. ATL, BB, MT, NO, PMZ, MSC, DRW, and PL contributed to the interpretation of the results. ATL took the lead in writing the paper. All authors provided feedback on the paper.

Competing interests. At least one of the (co-)authors is a member of the editorial board of *Atmospheric Chemistry and Physics*. The peer-review process was guided by an independent editor, and the authors also have no other competing interests to declare.

Acknowledgements. Andrew T. Lambe thanks Anita Avery, Jordan Krechmer, Timothy Onasch (Aerodyne), and Shreya Suri (Georgia Tech) for experimental assistance; Evgeni Glebov (Russian Academy of Sciences) for sharing published UV–Vis spectra of CAN / CH_3CN mixtures; and the following colleagues for helpful discussions: Harald Stark, Manjula Canagaratna (Aerodyne), Steve Brown (NOAA CSL), Hartmut Herrmann (TROPOS), William Brune (Pennsylvania State University), Tyson Berg (Colorado State University), Lasse Moormann (Max Planck Institute for Chemistry), Uta Wille (University of Melbourne), and Burkhard Koenig (University of Regensburg). The authors thank the anonymous referee and Sergey A. Nizkorodov for their constructive comments during the paper review process.

Financial support. This work was supported by the Atmospheric Chemistry Program of the US National Science Foundation (grant nos. AGS-2131368, AGS2148439, AGS-2131458, AGS-2131084, and AGS-2147893).

Review statement. This paper was edited by Sergey A. Nizkorodov and reviewed by Sergey A. Nizkorodov and one anonymous referee.

References

Alexander, A. J.: Reaction kinetics of nitrate radicals with terpenes in solution studied by cavity ring-down spectroscopy, Chem. Phys. Lett., 393, 138–142, https://doi.org/10.1016/j.cplett.2004.06.027, 2004.

Atkinson, R.: Kinetics and Mechanisms of the Gas-Phase Reactions of the NO_3 Radical with Organic Compounds, J. Phys. Chem. Ref. Data, 20, 459–507, https://doi.org/10.1063/1.555887, 1991.

Atkinson, R., Arey, J., Zielinska, B., and Aschmann, S. M.: Kinetics and nitro-products of the gas-phase OH and NO_3 radical-initiated reactions of naphthalene-d8, fluoranthene-d10, and pyrene, Int. J. Chem. Kinet., 22, 999–1014, https://doi.org/10.1002/kin.550220910, 1990.

Baciocchi, E., Del Giacco, T., Murgia, S., and Sebastiani, G.: The photochemical reaction of cerium(IV) ammonium nitrate with alkenes. Rate and mechanism for the addition of the nitrate radical to alkenes, Tetrahedron, 44, 6651–6660, https://doi.org/10.1016/S0040-4020(01)90103-6, 1988.

Bedjanian, Y.: Temperature-dependent rate constant for the reaction of F atoms with HNO_3, Int. J. Chem. Kinet., 51, 753–759, https://doi.org/10.1002/kin.21306, 2019.

Bertram, T. H., Kimmel, J. R., Crisp, T. A., Ryder, O. S., Yatavelli, R. L. N., Thornton, J. A., Cubison, M. J., Gonin, M., and Worsnop, D. R.: A field-deployable, chemical ionization time-of-flight mass spectrometer, Atmos. Meas. Tech., 4, 1471–1479, https://doi.org/10.5194/amt-4-1471-2011, 2011.

Birks, J. W., Andersen, P. C., Williford, C. J., Turnipseed, A. A., Strunk, S. E., Ennis, C. A., and Mattson, E.: Folded tubular photometer for atmospheric measurements of NO_2 and NO, Atmos. Meas. Tech., 11, 2821–2835, https://doi.org/10.5194/amt-11-2821-2018, 2018.

Blaustein, B. D. and Gryder, J. W.: An Investigation of the Species Existing in Nitric Acid Solutions Containing Cerium(III) and Cerium(IV)1, J. Am. Chem. Soc., 79, 540–547, https://doi.org/10.1021/ja01560a012, 1957.

Brown, S. S. and Stutz, J.: Nighttime radical observations and chemistry, Chem. Soc. Rev., 41, 6405–6447, https://doi.org/10.1039/C2CS35181A, 2012.

Brown, S. S., Dibb, J. E., Stark, H., Aldener, M., Vozella, M., Whitlow, S., Williams, E. J., Lerner, B. M., Jakoubek, R., Middlebrook, A. M., DeGouw, J. A., Warneke, C., Goldan, P. D., Kuster, W. C., Angevine, W. M., Sueper, D. T., Quinn, P. K., Bates, T. S., Meagher, J. F., Fehsenfeld, F. C., and Ravishankara, A. R.: Nighttime removal of NO_x in the summer marine boundary layer, Geophys. Res. Lett., 31, L07108, https://doi.org/10.1029/2004GL019412, 2004.

Burrows, J. P., Tyndall, G. S., and Moortgat, G. K.: Absorption spectrum of NO_3 and kinetics of the reactions of NO_3 with NO_2, Cl, and several stable atmospheric species at 298 K, J. Phys. Chem., 89, 4848–4856, https://doi.org/10.1021/j100268a038, 1985.

Cabañas, B., Baeza, M. T., MartÍn, P., Salgado, S., Villanueva, F., Monedero, E., and Wirtz, K.: Products and Mechanism of the NO_3 Reaction with Thiophene, J. Atmos. Chem., 51, 317–335, https://doi.org/10.1007/s10874-005-3580-5, 2005.

Choidini, G., Rindone, B., Cariati, F., Polesello, S., Restelli, G., and Hjorth, J.: Comparison between the gas-phase and the solution reaction of the nitrate radical and methylarenes, Environ. Sci. Technol., 27, 1659–1664, https://doi.org/10.1021/es00045a024, 1993.

Claflin, M. S.: Role of Multiphase Chemistry on the Formation of Aerosol from the Reactions of Monoterpenes with NO_3 Radicals and O_3, PhD thesis, University of Colorado, https://scholar.colorado.edu/concern/graduate_thesis_or_dissertations/b5644r712 (last access: 30 October 2023), 2018.

Claflin, M. S. and Ziemann, P. J.: Identification and Quantitation of Aerosol Products of the Reaction of beta-Pinene with NO_3 Radicals and Implications for Gas- and Particle-Phase Reaction Mechanisms, J. Phys. Chem. A, 122, 3640–3652, https://doi.org/10.1021/acs.jpca.8b00692, 2018.

D'Anna, B., Andresen, Ø., Gefen, Z., and Nielsen, C. J.: Kinetic study of OH and NO_3 radical reactions with 14 aliphatic aldehydes, Phys. Chem. Chem. Phys., 3, 3057–3063, https://doi.org/10.1039/B103623H, 2001.

Demars, T. J., Bera, M. K., Seifert, S., Antonio, M. R., and Ellis, R. J.: Revisiting the Solution Structure of Ceric Ammonium Nitrate, Angew. Chem. Int. Edit., 54, 7534–7538, https://doi.org/10.1002/anie.201502336, 2015.

DeVault, M. P., Ziola, A. C., and Ziemann, P. J.: Products and Mechanisms of Secondary Organic Aerosol Formation from the NO_3 Radical-Initiated Oxidation of Cyclic and Acyclic Monoterpenes, ACS Earth Space Chem., 6, 2076–2092, https://doi.org/10.1021/acsearthspacechem.2c00130, 2022.

Dörich, R., Eger, P., Lelieveld, J., and Crowley, J. N.: Iodide CIMS and m/z 62: the detection of HNO_3 as NO_3^- in the presence of PAN, peroxyacetic acid and ozone, Atmos. Meas. Tech., 14, 5319–5332, https://doi.org/10.5194/amt-14-5319-2021, 2021.

Dubé, W. P., Brown, S. S., Osthoff, H. D., Nunley, M. R., Ciciora, S. J., Paris, M. W., McLaughlin, R. J., and Ravishankara, A. R.: Aircraft instrument for simultaneous, in situ measurement of NO_3 and N_2O_5 via pulsed cavity ring-down spectroscopy, Rev. Sci. Instrum., 77, 34–101, https://doi.org/10.1063/1.2176058, 2006.

Gaillard de Sémainville, P., Hoffmann, D., George, C., and Herrmann, H.: Study of nitrate radical (NO_3) reactions with carbonyls and acids in aqueous solution as a function of temperature, Phys. Chem. Chem. Phys., 9, 958–968, https://doi.org/10.1039/B613956F, 2007.

Ganske, J. A., Wingen, L. M., Perraud, V., and Finlayson-Pitts, B. J.: Role of Gas-Phase Halogen Bonding in Ambient Chemical Ionization Mass Spectrometry Utilizing Iodine, ACS Earth Space Chem., 3, 1315–1328, https://doi.org/10.1021/acsearthspacechem.9b00030, 2019.

Glass, R. W. and Martin, T. W.: Flash generation and decay kinetics of the nitrate radical in aqueous nitric acid solutions, J. Am. Chem. Soc., 92, 5084–5093, https://doi.org/10.1021/ja00720a014, 1970.

Glebov, E. M., Grivin, V. P., Plyusnin, V. F., Fedunov, R. G., Pozdnyakov, I. P., Yanshole, V. V., and Vasilchenko, D. B.: Photochemistry of cerium(IV) ammonium nitrate (CAN) in acetonitrile, J. Photoch. Photobio. A, 418, 113440, https://doi.org/10.1016/j.jphotochem.2021.113440, 2021.

Henshall, A.: The Photoreduction of Ceric Ammonium Nitrate in Glacial Acetic Acid Solution, PhD thesis, Vanderbilt University, https://catalog.library.vanderbilt.edu/permalink/01VAN_INST/6ll2l/alma991025752059703276 (last access: 30 October 2023), 1963.

Hering, T., Slanina, T., Hancock, A., Wille, U., and König, B.: Visible light photooxidation of nitrate: the dawn of a nocturnal radical, Chem. Commun., 51, 6568–6571, https://doi.org/10.1039/C5CC01580D, 2015.

Hinsvark, O. N. and Stone, K. G.: Oxidation of Oxalic Acid in Glacial Acetic Acid with Cerium(IV), Anal. Chem., 28, 334–337, https://doi.org/10.1021/ac60111a014, 1956.

Jenkin, M. E., Saunders, S. M., Wagner, V., and Pilling, M. J.: Protocol for the development of the Master Chemical Mechanism, MCM v3 (Part B): tropospheric degradation of aromatic volatile organic compounds, Atmos. Chem. Phys., 3, 181–193, https://doi.org/10.5194/acp-3-181-2003, 2003.

Jiang, P. Y., Katsumura, Y., Ishigure, K., and Yoshida, Y.: Reduction potential of the nitrate radical in aqueous solution, Inorg. Chem., 31, 5135–5136, https://doi.org/10.1021/ic00050a038, 1992.

Kebabian, P. L., Herndon, S. C., and Freedman, A.: Detection of Nitrogen Dioxide by Cavity Attenuated Phase Shift Spectroscopy, Anal. Chem., 77, 724–728, 2005.

Krechmer, J., Lopez-Hilfiker, F., Koss, A., Hutterli, M., Stoermer, C., Deming, B., Kimmel, J., Warneke, C., Holzinger, R., Jayne, J., Worsnop, D., Fuhrer, K., Gonin, M., and de Gouw, J.: Evaluation of a New Reagent-Ion Source and Focusing Ion-Molecule Reactor for Use in Proton-Transfer-Reaction Mass Spectrometry, Anal. Chem., 90, 12011–12018, https://doi.org/10.1021/acs.analchem.8b02641, 2018.

Lambe, A. T., Krechmer, J. E., Peng, Z., Casar, J. R., Carrasquillo, A. J., Raff, J. D., Jimenez, J. L., and Worsnop, D. R.: HO_x and NO_x production in oxidation flow reactors via photolysis of isopropyl nitrite, isopropyl nitrite-d_7, and 1,3-propyl dinitrite at $\lambda = 254$, 350, and 369 nm, Atmos. Meas. Tech., 12, 299–311, https://doi.org/10.5194/amt-12-299-2019, 2019.

Lambe, A. T., Wood, E. C., Krechmer, J. E., Majluf, F., Williams, L. R., Croteau, P. L., Cirtog, M., Féron, A., Petit, J.-E., Albinet, A., Jimenez, J. L., and Peng, Z.: Nitrate radical generation via continuous generation of dinitrogen pentoxide in a laminar flow reactor coupled to an oxidation flow reactor, Atmos. Meas. Tech., 13, 2397–2411, https://doi.org/10.5194/amt-13-2397-2020, 2020.

Lee, B. H., Lopez-Hilfiker, F. D., Mohr, C., Kurten, T., Worsnop, D. R., and Thornton, J. A.: An Iodide-Adduct High-Resolution Time-of-Flight Chemical-Ionization Mass Spectrometer: Application to Atmospheric Inorganic and Organic Compounds, Environ. Sci. Technol., 48, 6309–6317, 2014.

Lopez-Hilfiker, F. D., Mohr, C., Ehn, M., Rubach, F., Kleist, E., Wildt, J., Mentel, Th. F., Lutz, A., Hallquist, M., Worsnop, D., and Thornton, J. A.: A novel method for online analysis of gas and particle composition: description and evaluation of a Filter Inlet for Gases and AEROsols (FIGAERO), Atmos. Meas. Tech., 7, 983–1001, https://doi.org/10.5194/amt-7-983-2014, 2014.

Martin, T. W. and Glass, R. W.: Competitive electron transfer. Activity-defined formation constants of cerium(III) nitrate complexes based on reaction with the nitrate free radical, J. Am. Chem. Soc., 92, 5075–5083, https://doi.org/10.1021/ja00720a013, 1970.

Martin, T. W. and Stevens, M. V.: Studies Using a Combination of Flash Photolysis and Pulsed Magnetic Induction: Application to the NO_3 Radical in Aqueous Acid Solution at 25 °C, in: 12th Informal Conference on Photochemistry, Gaithersburg, Maryland, United States of America, 28 June–1 July 1976, National Bureau of Standards Special Publication 526, https://doi.org/10.6028/NBS.SP.526, 1978.

Martin, T. W., Henshall, A., and Gross, R. C.: Spectroscopic and Chemical Evidence for the NO_3 Free Radical in Solution at Room Temperature, J. Am. Chem. Soc., 85, 113–114, https://doi.org/10.1021/ja00884a027, 1963.

Martin, T. W., Rummel, R. E., and Gross, R. C.: Electron Exchange Kinetics of the NO_3 Free Radical in Solution, J. Am. Chem. Soc., 86, 2595–2600, https://doi.org/10.1021/ja01067a016, 1964.

Meyer, R. J. and Jacoby, R.: Die Doppelnitrate des vierwertigen Ceriums und des Thoriums, Z. Anorg. Chem., 27, 359–389, https://doi.org/10.1002/zaac.19010270131, 1901.

Nah, T., Sanchez, J., Boyd, C. M., and Ng, N. L.: Photochemical Aging of α-pinene and β-pinene Secondary Organic Aerosol formed from Nitrate Radical Oxidation, Environ. Sci. Technol., 50, 222–231, https://doi.org/10.1021/acs.est.5b04594, 2016.

Nair, V. and Deepthi, A.: Cerium(IV) Ammonium NitrateA Versatile Single-Electron Oxidant, Chem. Rev., 107, 1862–1891, https://doi.org/10.1021/cr068408n, 2007.

Ng, N. L., Brown, S. S., Archibald, A. T., Atlas, E., Cohen, R. C., Crowley, J. N., Day, D. A., Donahue, N. M., Fry, J. L., Fuchs, H., Griffin, R. J., Guzman, M. I., Herrmann, H., Hodzic, A., Iinuma, Y., Jimenez, J. L., Kiendler-Scharr, A., Lee, B. H., Luecken, D. J., Mao, J., McLaren, R., Mutzel, A., Osthoff, H. D., Ouyang, B., Picquet-Varrault, B., Platt, U., Pye, H. O. T., Rudich, Y., Schwantes, R. H., Shiraiwa, M., Stutz, J., Thornton, J. A., Tilgner, A., Williams, B. J., and Zaveri, R. A.: Nitrate radicals and biogenic volatile organic compounds: oxidation, mechanisms, and organic aerosol, Atmos. Chem. Phys., 17, 2103–2162, https://doi.org/10.5194/acp-17-2103-2017, 2017.

Orlando, J. J. and Tyndall, G. S.: Laboratory studies of organic peroxy radical chemistry: an overview with emphasis on recent issues of atmospheric significance, Chem. Soc. Rev., 41, 6294–6317, https://doi.org/10.1039/C2CS35166H, 2012.

Palm, B. B., Campuzano-Jost, P., Ortega, A. M., Day, D. A., Kaser, L., Jud, W., Karl, T., Hansel, A., Hunter, J. F., Cross, E. S., Kroll, J. H., Peng, Z., Brune, W. H., and Jimenez, J. L.: In situ secondary organic aerosol formation from ambient pine forest air using an oxidation flow reactor, Atmos. Chem. Phys., 16, 2943–2970, https://doi.org/10.5194/acp-16-2943-2016, 2016.

Peng, Z. and Jimenez, J. L.: KinSim: A Research-Grade, User-Friendly, Visual Kinetics Simulator for Chemical-Kinetics and Environmental-Chemistry Teaching, J. Chem. Educ., 96, 806–811, https://doi.org/10.1021/acs.jchemed.9b00033, 2019.

Peng, Z. and Jimenez, J. L.: KinSim_Code, GitLab [code], https://gitlab.com/JimenezGroup/KinSim_Code, last access: 8 February 2023.

Sander, S., Abbatt, J. P. D., Barker, J. R., Burkholder, J. B., Friedl, R. R., Golden, D. M., Huie, R. E., Kolb, C. E., Kurylo, M. J., Moortgat, G. K., Orkin, V. L., and Wine, P. H.: Chemical Kinetics and Photochemical Data for Use in Atmospheric Studies, Evaluation Number 17, JPL Publication 10-6, https://jpldataeval.jpl.nasa.gov/pdf/JPL%2010-6%20Final%2015June2011.pdf (last access: 30 October 2023), 2011.

Saunders, S. M., Jenkin, M. E., Derwent, R. G., and Pilling, M. J.: Protocol for the development of the Master Chemical Mechanism, MCM v3 (Part A): tropospheric degradation of non-aromatic volatile organic compounds, Atmos. Chem. Phys., 3, 161–180, https://doi.org/10.5194/acp-3-161-2003, 2003.

Schwab, J. J., Brune, W. H., and Anderson, J. G.: Kinetics and mechanism of the hydroxyl + hydroperoxyl reaction, J. Phys. Chem., 93, 1030–1035, https://doi.org/10.1021/j100340a005, 1989.

Shen, H., Zhao, D., Pullinen, I., Kang, S., Vereecken, L., Fuchs, H., Acir, I.-H., Tillmann, R., Rohrer, F., Wildt, J., Kiendler-Scharr, A., Wahner, A., and Mentel, T. F.: Highly Oxygenated Organic Nitrates Formed from NO_3 Radical-Initiated Oxidation of β-Pinene, Environ. Sci. Technol., 55, 15658–15671, https://doi.org/10.1021/acs.est.1c03978, 2021.

Takeuchi, M. and Ng, N. L.: Chemical composition and hydrolysis of organic nitrate aerosol formed from hydroxyl and nitrate radical oxidation of α-pinene and β-pinene, Atmos. Chem. Phys., 19, 12749–12766, https://doi.org/10.5194/acp-19-12749-2019, 2019.

Veres, P. R., Roberts, J. M., Wild, R. J., Edwards, P. M., Brown, S. S., Bates, T. S., Quinn, P. K., Johnson, J. E., Zamora, R. J., and de Gouw, J.: Peroxynitric acid (HO_2NO_2) measurements during the UBWOS 2013 and 2014 studies using iodide ion chemical ionization mass spectrometry, Atmos. Chem. Phys., 15, 8101–8114, https://doi.org/10.5194/acp-15-8101-2015, 2015.

Wagner, N. L., Dubé, W. P., Washenfelder, R. A., Young, C. J., Pollack, I. B., Ryerson, T. B., and Brown, S. S.: Diode laser-based cavity ring-down instrument for NO_3, N_2O_5, NO, NO_2 and O_3 from aircraft, Atmos. Meas. Tech., 4, 1227–1240, https://doi.org/10.5194/amt-4-1227-2011, 2011.

Wang, H., Wang, H., Lu, X., Lu, K., Zhang, L., Tham, Y. J., Shi, Z., Aikin, K., Fan, S., Brown, S. S., and Zhang, Y.: Increased night-time oxidation over China despite widespread decrease across the globe, Nat. Geoscience, 16, 217–223, https://doi.org/10.1038/s41561-022-01122-x, 2023.

Wayne, R., Barnes, I., Biggs, P., Burrows, J., Canosa-Mas, C., Hjorth, J., Le Bras, G., Moortgat, G., Perner, D., Poulet, G., Restelli, G., and Sidebottom, H.: The nitrate radical: Physics, chemistry, and the atmosphere, Atmos. Environ. A-Gen., 25, 1–203, https://doi.org/10.1016/0960-1686(91)90192-A, 1991.

Wine, P. H., Mauldin, R. L., and Thorn, R. P.: Kinetics and spectroscopy of the nitrogen oxide radical (NO_3) in aqueous ceric nitrate-nitric acid solutions, J. Phys. Chem., 92, 1156–1162, https://doi.org/10.1021/j100316a031, 1988.

Wylie, A. W.: Extraction of ceric nitrate by solvents, J. Chem. Soc., 1474–1480, https://doi.org/10.1039/JR9510001474, 1951.